

# Autonomous Sensing and Control of Wing Stall Using a Smart Plasma Slat

Mehul P. Patel\* and Zak H. Sowler†  
*Orbital Research, Inc., Cleveland, Ohio 44103-3733*

and

Thomas C. Corke‡ and Chuan He§  
*University of Notre Dame, Notre Dame, Indiana 46556*

DOI: 10.2514/1.24057

**The concept of a self-governing smart plasma slat for active sense and control of flow separation and incipient wing stall is presented. The smart plasma slat design involves the use of an aerodynamic plasma actuator on the leading edge of a two-dimensional NACA 0015 airfoil in a manner that mimics the effect of a movable leading-edge slat of a conventional high-lift system. The self-governing system uses a single high-bandwidth pressure sensor and a feedback controller to operate the actuator in an autonomous mode with a primary function to sense and control incipient flow separation at the wing leading edge and to delay incipient stall. Two feedback control techniques are investigated. Wind tunnel experiments demonstrate that the aerodynamic effects of a smart actuator are consistent with the previously tested open-loop actuator, in that stall hysteresis is eliminated, stall angle is delayed by 7 deg, and a significant improvement in the lift-to-drag ratio is achieved over a wide range of angles of attack. These feedback control approaches provide a means to further reduce power requirements for an unsteady plasma actuator for practical air vehicle applications. The smart plasma slat concept is well suited for the design of low-drag, quiet, high-lift systems for fixed-wing aircraft and rotorcraft.**

## Nomenclature

$C_L$	=	coefficient of lift
$C_{L,max}$	=	maximum coefficient of lift
$c$	=	airfoil chord length
$F^+$	=	nondimensional frequency of actuator
$f$	=	modulation frequency of actuator
$L/D$	=	ratio of lift to drag
$L_{sep}$	=	extent of flow separation
$Re$	=	Reynolds number
$Re^{(chord)}$	=	Reynolds number based on length $c$
$Str$	=	Strouhal number
$t$	=	airfoil maximum thickness
$U_\infty$	=	freestream velocity
$x$	=	distance measured from the leading edge
$\alpha$	=	angle of attack, deg
$\alpha_{stall}$	=	stall angle, deg

## Introduction

**H**IGH-LIFT systems play an important role in the design of air vehicles. The wings on most modern-day air vehicles are equipped with high-lift systems, generally in the form of leading-edge slats and trailing-edge flaps. These devices have been shown to enhance the aerodynamic performance of air vehicles through increasing the maximum coefficient of lift, lift-to-drag ratio, and stall angle. Advantages of such performance-enhancing devices include

improvements in maneuverability, turn rates, glide range and payload, and reductions in takeoff/landing distance and field length requirements.

Although the benefits of high-lift devices are well documented in the open literature, it is also known that the use of movable control surfaces increases airframe noise and vibration, especially at high deflection angles. At these conditions, most of the noise originates from the separated flow in the gap regions which contribute to the form drag component of the viscous drag of the wing. At off-design conditions, in particular, the drag penalty from these devices is very high. By present estimates used in the wing and tail design, eliminating the hinge gaps would result in a 10% drag decrease [1]. Another drawback of movable control surfaces is that a deploy and retract mechanism is required, which adds volume, weight, and cost to the high-lift system. To enhance the aerodynamic and structural performance of the air vehicle, it is therefore desired to either fully replace the traditional movable control surfaces with hingeless devices that retain/improve the aerodynamic effects, or limit their deflection angles, without compromising lift performance.

Owing to the rapid growth in instrumentation, materials, and control technologies, the roles and capabilities of flow control and aerostructures are evolving. The use of smart aerostructures that can react rapidly to changing flow conditions to improve the aerodynamic and structural efficiencies of aircraft is gaining momentum. It is envisioned that future air vehicle designs will involve surfaces that shelter an integrated system of sensors, flow-control actuators, and feedback controllers that are able to adapt to unpredictable conditions (structural damage, wind shear, stall/spin, etc.) and reconfigure themselves in flight to regain/enhance control. This is the theme of the present work—the design of a smart aerostructure (slat) that can be used as an intelligent high-lift device with no moving parts.

This work presents the concept and experimental evaluation of a smart plasma slat: a low-drag, hingeless, high-lift device which uses a sensor, an aerodynamic plasma actuator, and a feedback controller for autonomous sense and control of leading-edge flow separation and wing stall. This paper reports follow on work towards the application of a (single-dielectric-barrier discharge) plasma actuator as a performance-enhancing device for a high-lift system. Previously, the effects of an “open-loop” plasma slat and plasma

Received 20 March 2006; revision received 1 August 2006; accepted for publication 1 August 2006. Copyright © 2006 by M. P. Patel and T. C. Corke. Published by the American Institute of Aeronautics and Astronautics, Inc., with permission. Copies of this paper may be made for personal or internal use, on condition that the copier pay the \$10.00 per-copy fee to the Copyright Clearance Center, Inc., 222 Rosewood Drive, Danvers, MA 01923; include the code 0021-8669/07 \$10.00 in correspondence with the CCC.

\*Director, Aerodynamics Group, 4415 Euclid Avenue, Suite 500. Senior Member AIAA.

†Aerospace Engineer, 4415 Euclid Avenue, Suite 500.

‡Clark Chair Professor, Aerospace and Mechanical Engineering Department, 101 Hessert Laboratory for Aerospace Research. Associate Fellow AIAA.

§Ph.D. Candidate, Aerospace and Mechanical Engineering Department, 101 Hessert Laboratory for Aerospace Research.

flap (plasma actuators applied on the wing leading edge and trailing edge, respectively) on the aerodynamic performance of a NACA 0015 were discussed [2]. The present work is focused on formulating self-governing methods to enable “closed-loop” operation of a plasma slat. Much of this work is focused on reducing the power levels of the plasma actuator for practical air vehicle applications, hence due consideration was given to the design of feedback control approaches that enable a continuous self-governing plasma actuator using a simple commercial off-the-shelf (COTS) pressure sensor. Wind tunnel experiments were conducted on a slowly pitching 2-D NACA 0015 airfoil to validate two different feedback control techniques designed for autonomous control. The designs are generic enough to be applied to any flow-control application where smart sensing and control of incipient flow separation is desired. The following sections provide a brief discussion of the different types of wing stall, plasma actuators, feedback control, and results from wind tunnel experiments.

### Wing Stall and Control

#### Wing Stall

The stall of a wing is a very complex problem and still remains one of the most important phenomena in aerodynamics. It occurs when the wing is unable to generate sufficient lift to keep the air vehicle in the air which can happen if the vehicle speed is too slow and/or if the angle of attack is too sharp, causing the flow to separate at the leading edge. Flow separation occurs when the boundary layer lifts off or separates from the surface of the wing under the influence of viscous forces and adverse pressure gradients acting within the boundary layer or due to geometrical aberrations [3,4]. Such low velocity and high  $\alpha$  conditions are usually encountered during takeoff and landing. Because of the large energy losses associated with boundary-layer separation, the performance of lifting surfaces is often deteriorated; hence the use of effective high-lift systems is crucial during such conditions.

One way of delaying wing stall is by using a high-lift device such as a leading-edge slat. It consists of a moving surface on the lower side of the wing that extends out ahead of the wing leading edge. Its primary effect is to increase  $\alpha_{stall}$  and  $C_{L,max}$  by allowing air from the high-pressure lower surface to circulate over the upper surface, which energizes the boundary layer and prevents flow separation, and therefore stall. Other examples of mechanical high-lift devices include a droop nose, Krueger flap, slotted Krueger flap, and a slotted slat. These hinged high-lift devices are effective, to varying degrees, in extending the  $\alpha_{stall}$  and  $C_{L,max}$  of the airfoil, however, they also add parasitic drag, weight, cost, and mechanical complexity to the high-lift system.

Flow control offers alternative methods of separation control using low-power hingeless devices. Some of the previously demonstrated flow-control methods for controlling flow separation include periodic excitation [5,6], passive and active vortex generators [7,8], and pulsed jet actuators [9]. In this work, a relatively new type of flow-control device, an aerodynamic plasma actuator [10], is used for controlling leading-edge flow separation and wing stall using feedback control. Because the present work deals with formulation based on the detection of flow characteristics (bubble formation, adverse pressure gradient, etc.) associated with separated flows, it seems relevant to first touch on the subject of wing stall.

#### Types of Stall

Decades of research in understanding the different stalling characteristics and their relation to the state of the boundary layer has led to a generalization of three types of stall that are widely accepted today for low-speed flows, albeit their demarcation calls for a more careful examination. These include 1) the thin-airfoil stall, where there is a gradual loss of lift at low lift coefficients as the turbulent reattachment point moves rearward; 2) the leading-edge stall, where there is an abrupt loss of lift, as the angle of attack for maximum lift is exceeded, with little to no rounding over the lift curves; and 3) the trailing-edge stall, where there is a gradual loss of lift at high  $C_L$  as the

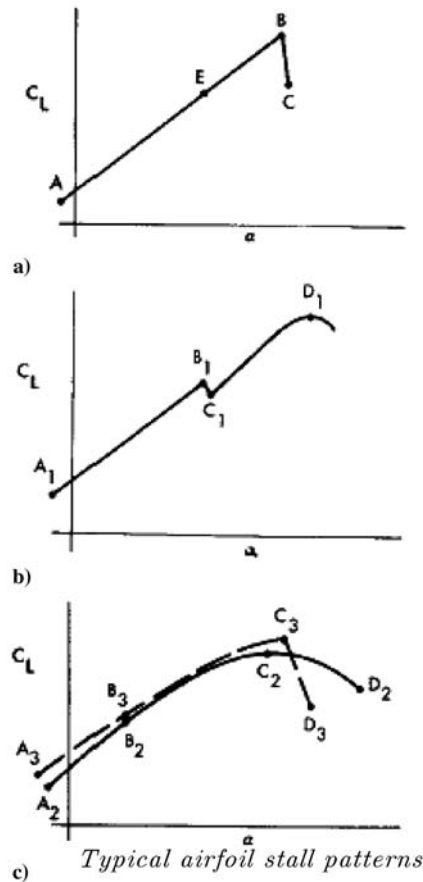
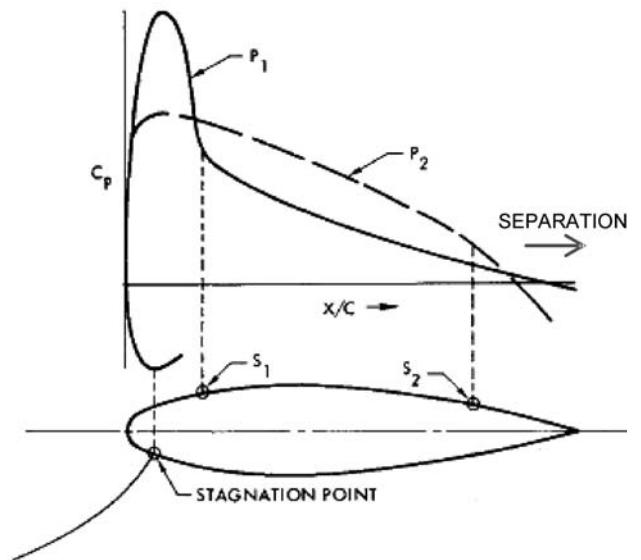


Fig. 1 Shape of the pressure distribution and typical airfoil stall patterns for single-element airfoil [11].

turbulent separation point moves forward from the trailing edge. Figure 1, adopted from [11], shows a typical pressure distribution for a single-component airfoil exhibiting either laminar stall (short and long bubble stall) or turbulent stall (trailing-edge stall) on the left, and the typical lift curves for the airfoils exhibiting laminar short bubble stall, laminar long bubble stall, and turbulent or trailing-edge stall for single-element airfoils on the right [11]. In Fig. 1,  $P_1$  = pressure distribution for incipient laminar stall (short bubble and long bubble);  $P_2$  = pressure distribution for incipient turbulent stall (trailing-edge stall);  $S_1$  = point of incipient laminar separation and reattachment or laminar separation only; and  $S_2$  = point of incipient turbulent separation. Figure 1a shows the laminar short bubble at  $S_1$

bursts and  $C_L$  drops abruptly from  $B$  to  $C$ ; Fig. 1b shows the laminar long bubble at  $S_1$  develops into an extended region of separation for  $C_L$ s between  $C_1$  and  $D_1$ , where flow is unstable; and Fig. 1c shows the turbulent trailing edge stall.  $A_2B_2C_2D_2$  boundary layer changes from laminar to transition to turbulent and then separates at  $C_2$ .  $A_3B_3C_3D_3$  boundary layer progresses from laminar to local separation, then to turbulent reattachment, and finally to turbulent separation.

Laminar stall is caused as a result of a very high suction peak and succeeding high adverse pressure gradient near the leading edge, whereas turbulent stall occurs as a result of a relatively high adverse pressure gradient near the aft part of airfoil. The flows associated with thin-airfoil stall and leading-edge stall are characterized by the accompanying separation bubble. When the laminar boundary layer separates from the surface of the airfoil, the resulting separated shear layer may curve back onto the airfoil surface within a short distance. The region of circulatory motion underneath a separated flow between points of separation and reattachment is defined as a “short bubble.” In certain cases, however, the separated viscous layer, which is formed in the neighborhood of the location of minimum peak pressure on the airfoil, may not reattach to the surface at all or may reattach after 0.2–0.3 chord lengths downstream. In either case, the flow over the airfoil is unsteady because of the presence of the large region of circulatory motion underneath the separated flow. The extended separated region is defined as a “long separation bubble.” The presence of the short laminar separation bubble near the leading edge of the airfoil may give rise to laminar stall. This type of stall is distinguished from the turbulent or trailing-edge stall by the fact that in the case of trailing-edge stall, turbulent boundary-layer separation takes place near the aft end of the airfoil causing the existence of a sizable region of separated flow.

A laminar separation bubble is either called short or long depending on the magnitude of  $R_e$  (based on velocity and momentum thickness of boundary-layer separation) and pressure gradient. If the bubble is short and the angle of attack is then increased, the separation point moves forward to a region of increasing surface curvature. Eventually turbulent reattachment of the full shear layer fails to take place, and there is a consequent sudden loss of lift and increase in drag. Separation involving formation of a short bubble can occur on most conventional airfoil sections of moderate thickness to chord ratio in the range of  $0.09 < t/c < 0.15$ .

If the bubble is long, then an increase in the angle of attack produces a progressive rearward movement of the reattachment, thus increasing the length of the bubble until it coincides with the trailing edge. Stall is reached at about this angle of attack; any further increase in  $\alpha$  results in a gradual reduction in lift. This separation process can also occur on most conventional thin airfoils having  $t/c$  ratios up to about 0.09, and it is usually called thin-airfoil stall. Aerodynamically, whereas the formation and development of a long bubble has a considerable adverse effect on drag via the pressure distribution, the existence of a short bubble has a negligible effect up to the harmful stall condition.

The turbulent separation from the trailing edge is characteristic of most conventional thick airfoil sections in a range of  $t/c$  greater than 0.12. An increase in angle of attack produces a gradual forward movement of the point of separation and steady and gradual decrease in lift. It is possible for both short bubble and trailing-edge separation to exist on the same families of airfoils at the same time over a certain range of  $R_e$ . The former generally starts to develop at a lower angle of attack than does the latter. This combination of separation consequently displays characteristics of both short bubble and the trailing-edge separation, with the possibility of either a semirounded lift curve peak followed by an abrupt decrease in lift or a relative sharp lift curve peak followed by a relatively rapid decrease in lift.

In all cases, the flow over the wing is unsteady because of the presence of the large region of circulatory motion underneath the separated flow. The ultimate goal of the present work is to develop methods to identify incipient flow separation by correlating pressure fluctuations with physical phenomena (bubble formation, wind gusts, etc.) which can be used as a feedback rule for switching the plasma actuator on or off for autonomous control. In this work, we

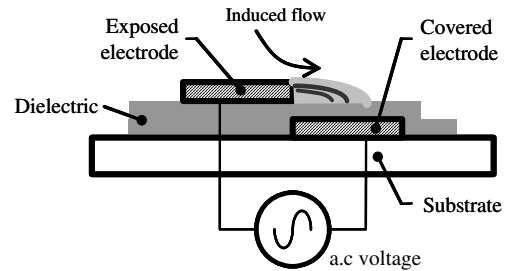


Fig. 2 Asymmetric electrode arrangement of an aerodynamic plasma actuator.

investigate a slowly pitching two-dimensional NACA 0015 airfoil and capture the pressure fluctuations near the wing leading edge using a high-bandwidth pressure sensor located just downstream of the leading-edge plasma actuator (at  $x/c = 0.05$ ) to detect incipient flow separation. Two feedback control methods are developed: 1) amplitude peak sense and control (APSC), and 2) pressure amplitude sense and control (PASC). The former relies on the detection of actuator frequency peaks in the flowfield under the influence of an upstream unsteady actuator, and the latter relies on the detection of high amplitude peaks over ranges of key preselected frequencies that exhibit strong characteristics of incipient flow separation. Wind tunnel experiments are conducted to validate both methods of feedback control.

#### Aerodynamic Plasma Actuator

An aerodynamic plasma actuator is a particular configuration of the dielectric-barrier discharge (a surface discharge) which consists of two electrodes that are separated by a dielectric material. One of the electrodes is typically exposed to the surrounding air and the other is fully encapsulated by a dielectric material, as shown in Fig. 2. When an a.c. voltage (5 kHz) is supplied to the electrodes, at sufficiently high amplitude levels (3–12 kV peak to peak), the air ionizes in the region of the largest electric field potential. This typically occurs at the edge of the electrode that is exposed to the air and spreads out over the area projected by the covered electrode, directing momentum into the surrounding air.

The process of ionizing the air in this configuration is classically known as a single-dielectric-barrier discharge [12]. The basis of this plasma actuator configuration is that the ionized air (plasma) in the presence of an electric field gradient produces a body force on the ambient air [13], which induces a virtual aerodynamic shape over the surface around the actuator. The body-force vector can be tailored for a given application by configuring the orientation and design of the electrode geometry. The body-force representation is also a convenient form to incorporate the effect of the actuators in Navier–Stokes (NS) simulations, which are currently being used to design and predict the performance of plasma actuators for various applications [14–16].

An excellent review of the physics and the underlying mechanisms of the aerodynamic plasma actuator is provided by Enloe et al. [12,13]. The use of single-dielectric-barrier-discharge plasma actuators for flow-control applications has been demonstrated by several researchers. Examples of flow-control applications using plasma actuators include exciting 3-D boundary-layer instabilities on a sharp cone at Mach 3.5 [17], lift augmentation on wings [18], separation control for low-pressure turbine blades [19], leading-edge separation control on wing sections [20], phased plasma arrays for unsteady flow control [21], and control of the dynamic stall vortex on oscillating airfoils [22]. More recently, the use of plasma actuators has been demonstrated for air vehicle applications such as plasma flaps and slats [2] and plasma wing for hingeless flight control [23]. A new method to enhance the effects of a low-power “unsteady” plasma actuator are investigated using novel plasma-optimized airfoil design concepts [24].

The majority of the applications for plasma actuators referenced above deals with the control of flows in an open-loop mode. The authors were unable to find any work in the literature on the

experimental use of plasma actuators using feedback control before this work. To this end, this paper presents the first look into the use of smart plasma actuators for autonomous sense and control of separated flows. The two main outcomes of the present work are 1) a smart skin that can operate continuously in an autonomous mode to maintain the aerodynamic efficiency at optimum settings, and 2) reduction of power requirements for the plasma actuators by turning them off when they are either not necessary or would be ineffective.

In the present work, the plasma actuators used were made from two 0.0254 mm thick copper electrodes separated by two 0.1 mm (4-mil) thick Kapton film layers. The Kapton has a breakdown voltage of approximately 7 kV per  $10^{-3}$  in. thickness and a dielectric constant of 3.3, which provide good electrical properties. The electrodes were arranged in the asymmetric arrangement illustrated in Fig. 2. They were overlapped by a small amount (approximately 1 mm) to ensure a uniform plasma in the spanwise direction. The plasma actuator was bonded directly to the surface of the model. At the leading edge, where the flow is sensitive to the nose radius, a 0.1 mm recess was molded into the model to secure the actuator flush to the surface. The electrodes were positioned so that the junction between the exposed and covered electrodes was precisely at the leading edge. The actuator induced an accelerating velocity component in the mean freestream direction over the suction surface of the model.

The leading-edge plasma actuator, located at  $x/c = 0.0$ , was operated in an unsteady manner. The a.c. carrier frequency supplied to the electrodes was 5 kHz and the a.c. voltage supplied to the electrodes was on the order of 3–12 kV<sub>p-p</sub>. The power used by the actuator was approximately 2–4 W per linear foot of actuator span. In the unsteady mode, very short duty cycles are possible, which reduces the actuator power requirements significantly. For example, a 10% duty cycle provided results better than the “steady” operation which used 100% duty cycle. The unsteady actuator frequency  $f$  was determined based on a Strouhal number scaling of a dimensionless frequency,  $F^+ = fL_{sep}/U_\infty = 1$ . For all cases presented here, the unsteady modulation frequency of the actuator was 166 Hz and the actuator was operated at 10% duty cycle.

### Experimental Setup

The airfoil used for this study was a 2-D NACA 0015 (hereafter 0015) with a 12.7 cm (5-in.) chord and a 25.4 cm (10-in.) span. Photographs of the 0015 are shown in Fig. 3. The 0015 was chosen for study because its characteristics are well documented in the literature and the airfoil was also the subject of an experiment on dynamic stall control using plasma actuators, which provided flow visualization records (see Fig. 4) [22]. The size of the airfoil was a compromise between minimizing blockage effects, especially at high  $\alpha$  and maintaining a large enough chord Reynolds number,  $Re_{e(chord)}$ . At the largest angle of attack tested, that is,  $\alpha = 23$  deg, the blockage was 8.5%, which still ultimately required correction in the measured lift and drag coefficients. The airfoil was cast using an epoxy-based polymer in a two-piece mold. The mold was precisely machined using a numerical-controlled milling machine.

Experiments were conducted at  $Re_{e(chord)} = 1.8 \times 10^5$  ( $U_\infty = 21$  m/s) in a subsonic wind tunnel located in the Center for Flow Physics and Control (FlowPAC) in the Hessert Laboratory at the University of Notre Dame. The facility is an open-return draw-down wind tunnel with a 0.421 m  $\times$  0.421 m  $\times$  1.8 m (long) test section. The tunnel consists of a removable inlet with a series of 12 screens followed by a 24:1 contraction that attaches to the test section. The test section is equipped with a clear Plexiglas sidewall that allows optical access to view the model. The back wall of the test section has removable panels to allow access into the test section.

The 0015 used in the study was mounted vertically to the support sting of a lift-drag force balance on top of the test section. The airfoil was suspended between endplates that were attached parallel to the ceiling and floor of the test section. The endplates were designed to produce a two-dimensional flow around the airfoil. A hole in the ceiling endplate accommodated the sting supporting the airfoil. A

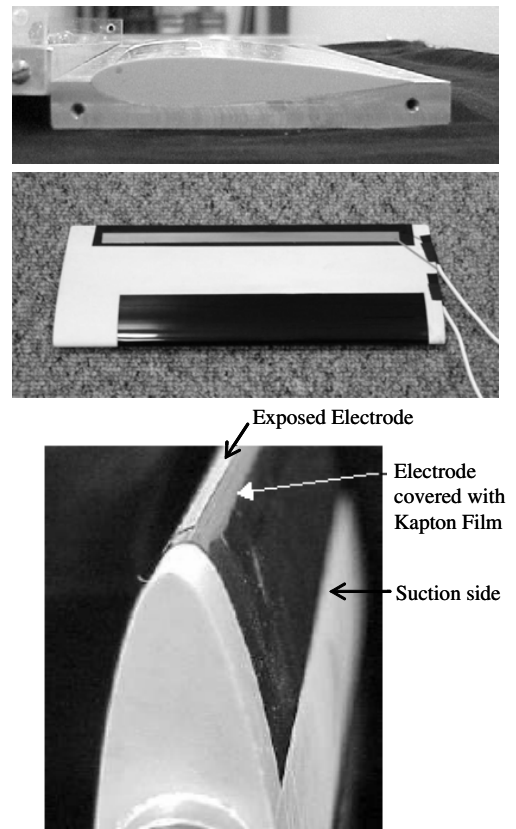


Fig. 3 Photographs of the 2-D NACA 0015 airfoil model.

hole in the floor endplate allowed access for the actuator wiring. This hole was aligned with the support sting so that it would not interfere with angular positioning of the airfoil when setting different angles of attack. A stepper motor on the force balance drove the angular

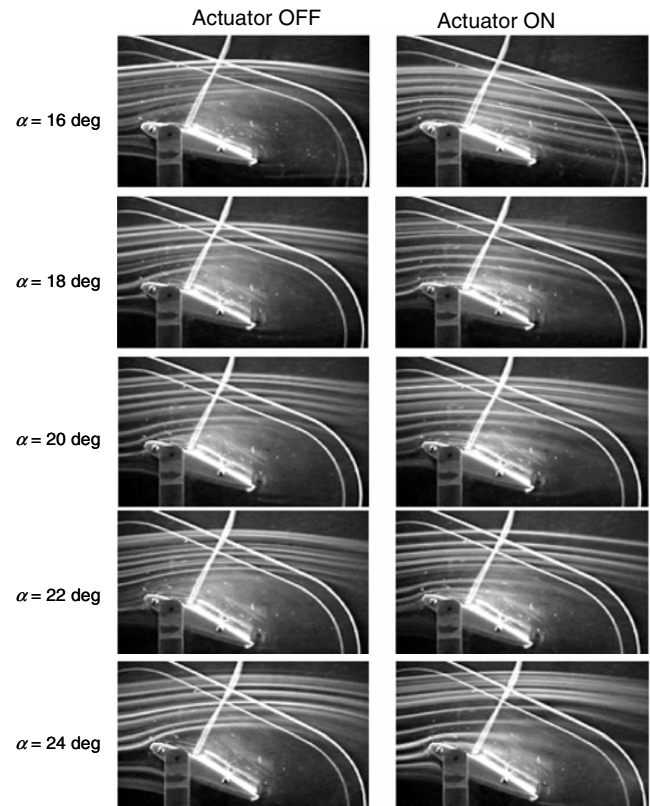


Fig. 4 Flow visualization records of the 2-D 0015 airfoil model with the steady leading-edge plasma actuator off and on [22].

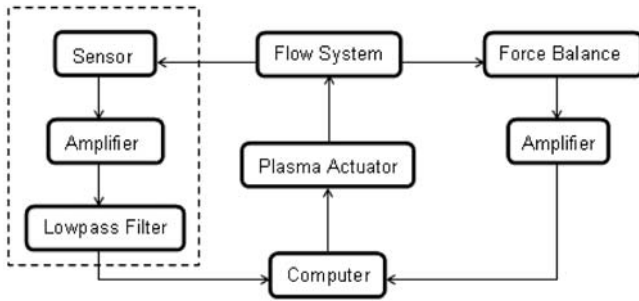


Fig. 5 Diagram of the smart plasma slat experimental system.

position of the support sting. Its motion was controlled by the data acquisition computer through software. With this, the angular position was repeatable to  $\pm 0.005$  deg. Figure 5 shows the diagram of the experimental system.

**Feedback Control**

Two methods of predicting incipient flow separation at the wing leading edge were developed based on the frequency and time domain analyses of the pressure data, which were then experimentally verified via closed-loop control experiments. The APSC method is based on the detection of frequency peaks in the flowfield under the influence of an upstream unsteady actuator, and the other PASC method relies on the detection of high amplitude peaks of key pressure frequencies that are strong precursors of flow separation. In both the approaches, we track incipient separation on the upper surface of the airfoil to predict stall. The plasma actuator was operated at an a.c. amplitude of 7 kV<sub>(p-p)</sub> and at a modulation frequency of 166 Hz ( $F^+ = 1$ ). Pressure data were sampled at 1 kHz, and lift and drag was measured on the wing using a force balance. Pressure measurements were made using a high-bandwidth pressure

sensor located at the leading edge,  $x/c = 0.05$ , on the suction side. This location was chosen to allow detection of incipient flow separation at the leading edge. Figure 6 shows the photograph and schematic of the airfoil model and the pressure sensor used in the experiments. As shown in Fig. 6, a slot was machined into the pressure side of the airfoil which was used to accommodate the sensor. The slot cavity was sealed by clear tape.

**Amplitude Peak Sense-and-Control (APSC) Method**

The diagram in Fig. 5 represents a block diagram for the APSC control method. To find the rule for feedback control, the characteristic of static pressure at  $x/c = 0.05$  was investigated at each angle of attack when the plasma was off and on. Figure 7 shows the fast Fourier transform (FFT) analysis of discrete sampled static pressure data at different angles of attack. For  $\alpha \leq 12$  deg there is no difference between the spectra with the plasma actuator off and on. However, when  $\alpha$  reaches 13 deg, which is 1 deg lower than the flow separates at the leading edge, a dominant frequency and its harmonic appears in the spectrum when the plasma actuator is on. This frequency corresponds to the unsteady forcing frequency of the plasma actuator which was 166 Hz in this case.

At  $\alpha = 14.5$  deg, which is immediately after  $\alpha_{stall}$ , a low-frequency dominates the flow when the actuator is off. This low frequency was investigated by Broeren and Bragg [25]. The results showed that the development and growth of the leading-edge

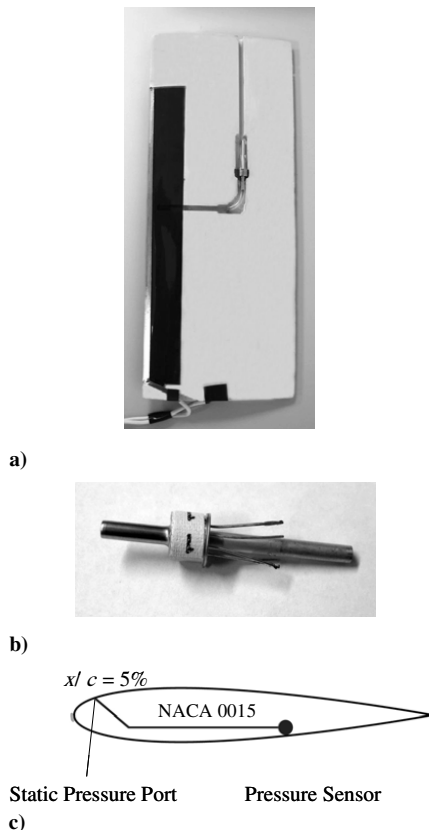


Fig. 6 a) Photograph of 2-D NACA 0015 airfoil model with a fast-response pressure sensor; b) close view of the pressure sensor; c) schematic of NACA 0015 airfoil with a pressure sensor and location of the pressure port.

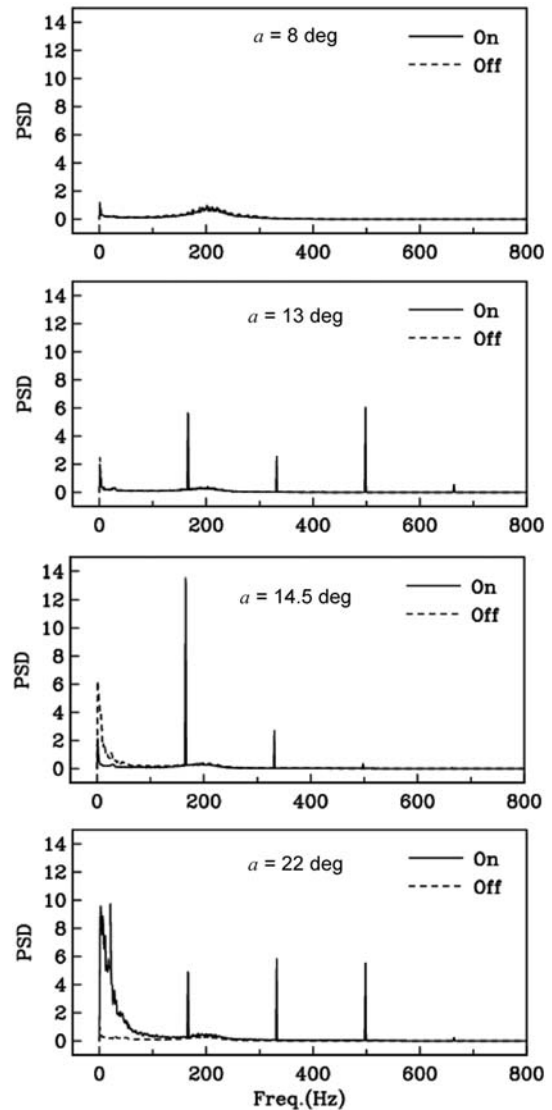


Fig. 7 Power spectrum of discrete sampled static pressure at  $\alpha = 8, 13, 14.5,$  and  $22$  deg when plasma actuator is turned off and on.

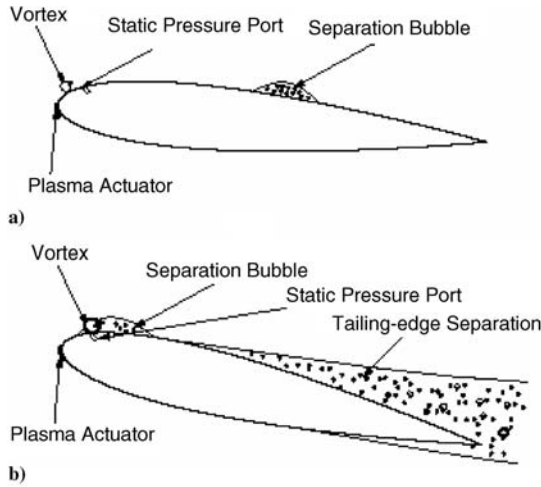


Fig. 8 a) Schematic of separation bubble position at  $\alpha < 13$  deg; b) schematic of interaction between separation bubble and vortex generated by the plasma actuator.

separation bubble that merges with the trailing-edge turbulent boundary-layer separation plays a key role in the low-frequency oscillation. When the plasma actuator is turned on, this low frequency vanishes and the spectral peak at 166 Hz again appears. A similar peak in the measured pressure spectrum is observed all the way up to  $\alpha = 23$  deg, which was the highest angle of attack investigated.

At a low angle of attack ( $\alpha < 13$  deg), just before the leading-edge stall, a small separation region (bubble) begins to form downstream of the sensing port at  $x/c = 0.05$ . This would be point S1 in Fig. 1. It is speculated that this location (S1) is just past the maximum thickness point of the 0015 ( $x/c = 0.3$ ), as illustrated in Fig. 8. The plasma actuator design and frequency operation were meant to force spanwise vortices that efficiently mix outer high-momentum fluid with the low-momentum fluid near the surface, causing the flow to reattach. At lower angles of attack, the flow at the leading edge is attached. When the plasma actuator is on, the strong favorable pressure gradient around the leading-edge nose damps the unsteady input from the actuator so that even close to the leading edge, just downstream of the actuator ( $x/c = 0.05$ ), the pressure fluctuations due to the actuator are not sensed.

As  $\alpha$  increases, the small separation bubble gradually moves forward until in the case of the present experiment, at  $\alpha = 13$  deg, S1 moves forward of the pressure sensor location. The small separation bubble is very receptive to the unsteady condition produced by the plasma actuator. As a result, the pressure sensor now shows a spectral peak at the actuator unsteady frequency. Note that this small separation bubble is a precursor of the full leading-edge separation

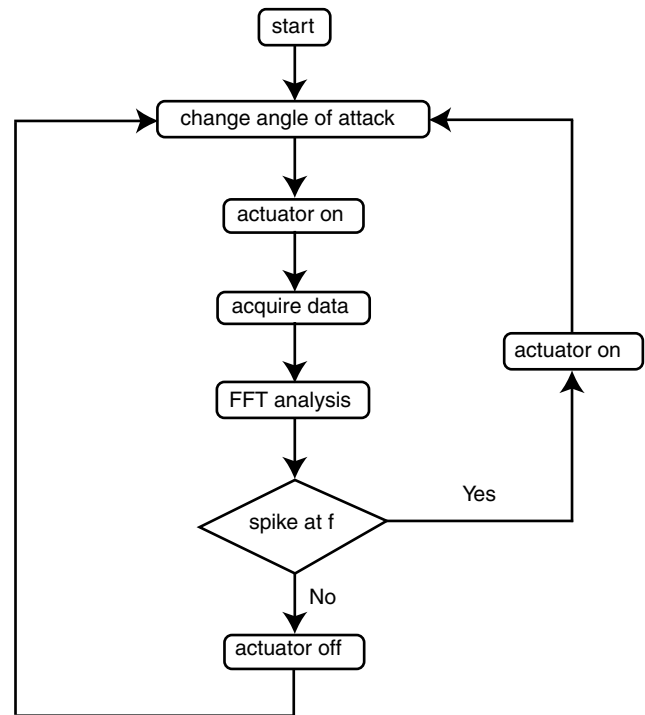


Fig. 9 Flowchart for the amplitude peak sense-and-control (APSC) feedback control method.

on this airfoil at low Reynolds number. Therefore, having it appear in the spectrum at prestall angles of attack provides a feedback signal to keep the actuator on.

The evidence of a separation bubble that occurs near the leading edge comes from two bits of information. The first is the observation that when the unsteady pressure was measured at the 10%  $c$  location, a larger  $\alpha$  (1.5–2 deg) precursor of stall was observed compared to the 1 deg  $\alpha$  precursor obtained with the unsteady pressure measurement measured at the 5% location. This indicates that the separation bubble was moving forward as the  $\alpha$  increased. The second indication of our interpretation was the prediction of a separation point between 5–10%  $c$  at a 13 deg  $\alpha$  obtained using the X-Foil program.

A more remarkable feature of this method of separation detection is that even after the flow has been reattached by the unsteady plasma actuator, the pressure sensor near the leading edge still senses a peak in the spectrum at the unsteady frequency as long as the flow will not attach naturally. However, even with the actuator on, if  $\alpha$  is low enough for the flow at the leading edge to be naturally attached, the spectral peak at the actuator frequency is not visible. Thus, this

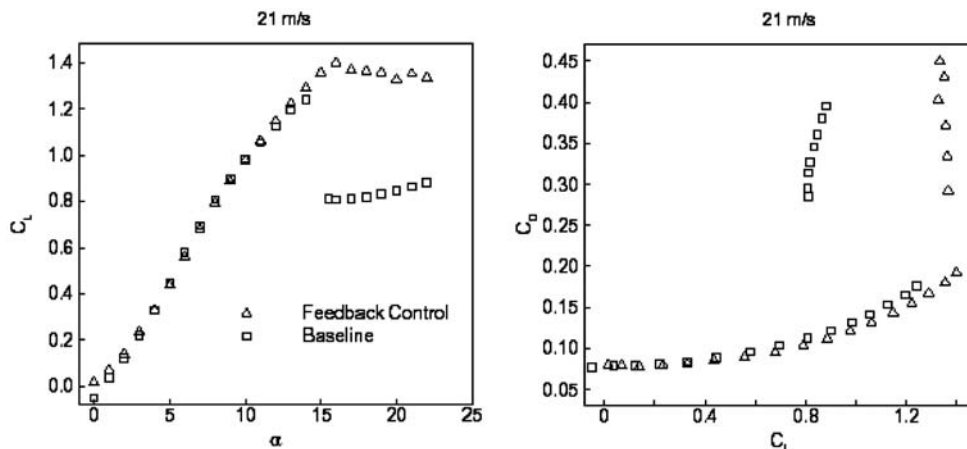


Fig. 10 Lift coefficient versus angle of attack and drag polar for the NACA 0015 airfoil at 21 m/s with APSC feedback control.

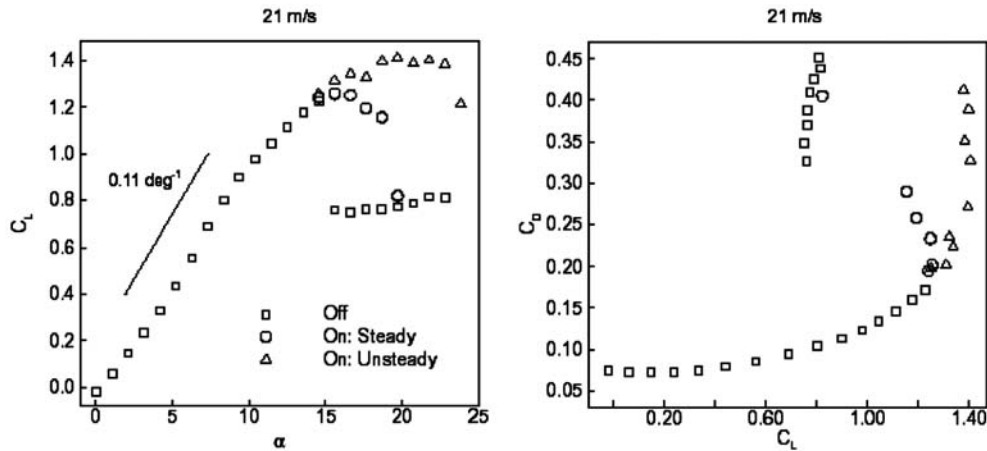


Fig. 11 Lift coefficient versus angle of attack and drag polar for the NACA 0015 airfoil at 21 m/s with the plasma actuator off (squares), steady on (circles), and unsteady on (triangles) operation [2].

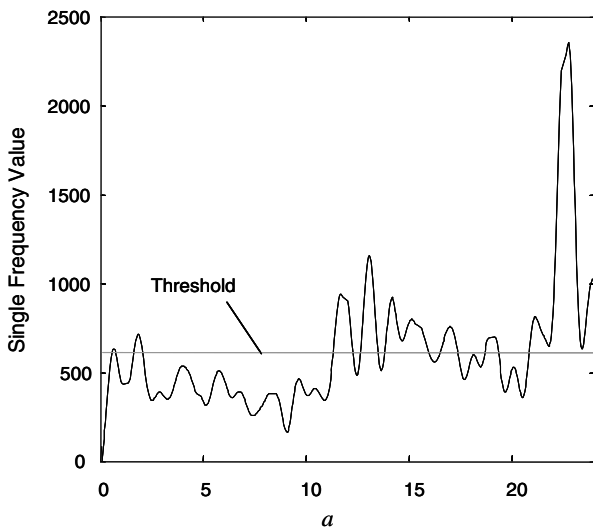


Fig. 12 A representative plot showing amplitude fluctuations of a single frequency bin from the pressure signal during the NACA 0015 airfoil pitch-up experiment.

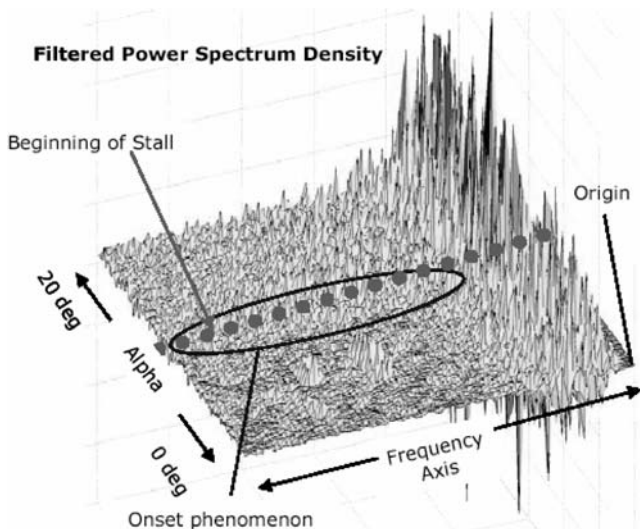


Fig. 13 Spectral power distribution plot showing frequency bins as a function of angle of attack and time during the NACA 0015 pitch-up experiment with the actuator off. A rise in the amplitude level of discrete frequency bins is observed at  $\alpha = 12$  deg before  $\alpha_{stall}$ , which occurs at  $\alpha = 14$  deg in this case with no control.

characteristic provides a method to both sense incipient separation to turn the actuator on, and sense when the actuator no longer needs to be on, saving actuator power.

Based on this explanation of the APSC, a control procedure shown in Fig. 9 is implemented. First, at any given  $\alpha$  of the airfoil, the unsteady plasma actuator is turned on, the pressure sensor time series is sampled, and the frequency spectrum is computed. If a spectral peak is found at the actuator unsteady forcing frequency, the flow is sensed to be close to separation, or at a large  $\alpha$  at which if the actuator were turned off, the flow would separate. Thus, the unsteady plasma actuator stays on. If the peak at the unsteady actuator frequency does not appear in the pressure spectra, the airfoil  $\alpha$  is low enough for the flow to be far from separating. In this case, the plasma actuator is turned off. This control loop is exercised every time  $\alpha$  is changed in the laboratory experiment. In a flight scenario, it would be operating autonomously in the control loop to always sense and control incipient separation.

A demonstration of the control procedure is presented in Fig. 10. This shows the lift coefficient versus  $\alpha$ , and drag polar for the baseline airfoil condition (actuator off) and for the feedback control of the actuator using the APSC approach. The results are indistinguishable from the open loop forcing for the same airfoil conditions by Corke et al. [2] with the same increase in  $\alpha_{stall}$  and  $L/D$ ; see Fig. 11. However, in this case (Fig. 10) the actuator is only operating when necessary, where in flight scenarios will ultimately use less energy compared to open-loop flow control. When the vortex generated by a plasma actuator goes through the separation bubble, it collects the energy that resides in small eddies in the separated turbulent boundary layer and becomes strong enough to be sensed by the pressure sensor. That causes the dominant frequency to appear in the power spectrum when the actuator is on. The stronger vortex brings high momentum fluid to the surface and keeps the separation bubble from bursting when the trailing-edge boundary-layer separation moves forward and emerges with the separation bubble as  $\alpha$  increases. After the stall, the lift coefficient continues to increase to  $C_{L(max)}$  and then drops very gradually instead of an abrupt decrease (see Fig. 10).

**Pressure Amplitude Sense-and-Control (PASC) Method**

Previous work by Patel et al.[8] has shown that a single high-bandwidth pressure sensor placed optimally on the surface of a wing can be used to detect incipient flow separation. In this earlier work, a standard deviation (STDEV) formulation based on the time- and frequency-domain analysis of the pressure data was used to predict flow separation and incipient stall. Using this feedback rule, active stall control of a slow-pitching 30-deg sweep NACA 0020 airfoil was demonstrated using a system of dynamic pressure sensors, leading-edge deployable vortex generators, and a closed-loop controller. The present PASC approach uses a more refined method of predicting separation/stall signature using the power spectrum density (PSD)

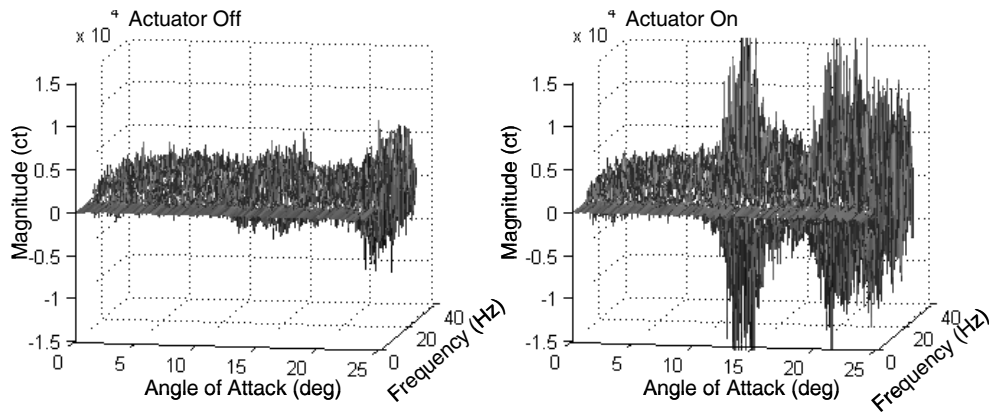


Fig. 14 Plots showing frequency versus angle of attack (and time) from the NACA 0015 airfoil pitch-up experiment with the unsteady leading-edge plasma actuator off (left) and on (right).

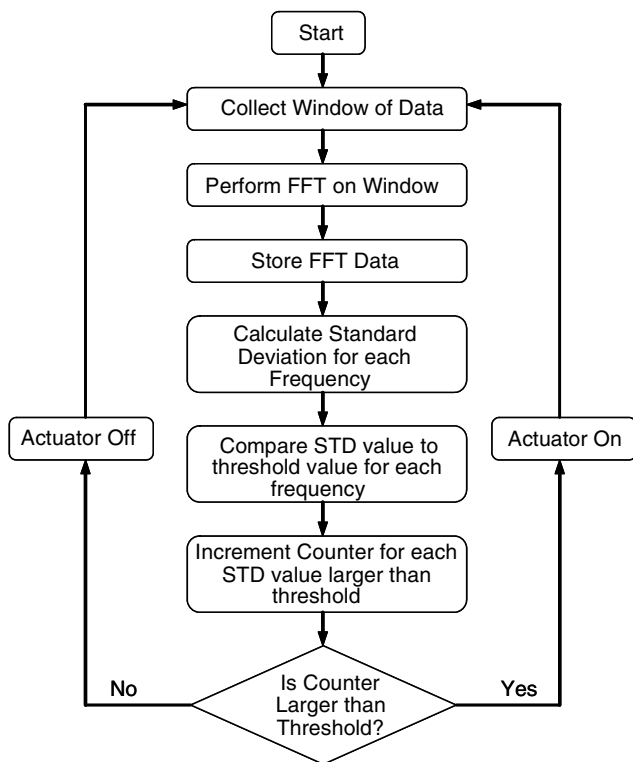


Fig. 15 Flowchart for the pressure amplitude sense-and-control (PASC) feedback control method.

analysis of discrete frequency bins of the pressure signal for feedback control, as opposed to looking at an aggregate of all frequencies, as was done in the STDEV technique [8].

The PASC method allows us to examine how the power (amplitude) of the pressure time series is distributed with frequency. A characteristic rise in the amplitude levels of pressure frequencies is measured before  $\alpha_{stall}$ , which is used as a precursor to the onset of stall phenomena. An increase in the amplitude (power) of the pressure signal is indicative of increased flow turbulence in the vicinity of the pressure sensor which is caused by high adverse pressure gradient and a separating flowfield. Identifying these precursors of flow separation at the wing leading edge enables the control system to activate the plasma actuator to control the flow separation and delay of  $\alpha_{stall}$ .

To demonstrate the performance of the smart plasma slat using the PASC approach, experiments were conducted on a slowly pitching 0015 ( $\pm 0.118$  deg/s) using a single pressure sensor at  $x/c = 0.05$  on the suction side. The experimental setup was exactly the same for

the APSC experiments. Pitching tests were conducted with the plasma actuator held off and on to capture the pressure fluctuations and the resulting lift and forces. Figure 12 shows an example of the characteristic rise in the amplitude of a single frequency bin (from a total of 64 bins that were examined) as the 0015 was pitched up from 0 to 24 deg at 0.1 deg/s. A detailed time- and frequency-domain analysis was conducted using the PASC method for all frequency bins captured during pitch-up and pitch-down experiments with the actuator held off and on. Frequency bins that featured promising trends in predicting the stall onset behavior (abrupt shifts in the amplitude levels) were identified for further analysis. The results from the PSD analysis are shown in Figs. 13 and 14. Figure 13 shows a spectral power distribution plot of the 0015 pitch-up case with the actuator off, and Fig. 14 shows a two-dimensional view of the spectral plot for the 0015 pitch-up case with the actuator off (left panel) and on (right panel). A characteristic rise in the amplitude levels is observed for the frequency bins near 60 Hz at  $\alpha = 12$  deg (indicated by a circle in Fig. 13, right) before stall which occurs at  $\alpha = 14$  deg in this case. These amplitude levels are higher in the actuator off case (Fig. 14, left) compared to the actuator on case (Fig. 14, right), which indicate that the actuator is highly effective in reattaching the flow (or reducing the bubble size) and reducing the large-scale flow structures in the flowfield.

Based on this explanation of the PASC method, a control system illustrated by the flowchart shown in Fig. 15 was implemented. First, the system selects a window of data, filters out low-frequency phenomena, and performs a FFT on the windowed data. Then it stores each transformed window as a row in a first-in-first-out (FIFO) stack. Each column in that FIFO stack represents the component of the signal at that time within a narrow frequency range. The STDEV of the preselected columns or “bins” is then calculated and compared to a predetermined “threshold”; if more than a predetermined fraction of the bins exceeds their respective thresholds, then the actuator state is set to on, or else the actuator state is set to off. Certain frequencies that exhibit a characteristic rise in the amplitude are selected and analyzed to identify specific threshold values to change the sensitivity/robustness of the controller.

It is found that if more threshold values are used to trigger the actuators in feedback control, the system becomes insensitive to faulty precursors (see Fig. 16). Examples of this are shown in Fig. 16 where the controller activity (triggering the actuator off and on) is compared for different frequency-bin and threshold settings during pitch-up and pitch-down experiments. This clearly shows that when the controller used only two frequency bins to monitor the flow, it was highly sensitive to the flow instabilities and turned the actuator on upon detecting the slightest instability (relatively speaking) in the amplitude (power) at those frequencies. As more and more frequency bins were added to the “stall detection” analysis portion of the PASC code, the controller became more robust and less sensitive to the flow instabilities, and it turned the actuator off and on only when “true” onset to stall was detected. This was verified experimentally as shown in Fig. 16 by comparison of the control off/on state in the top,

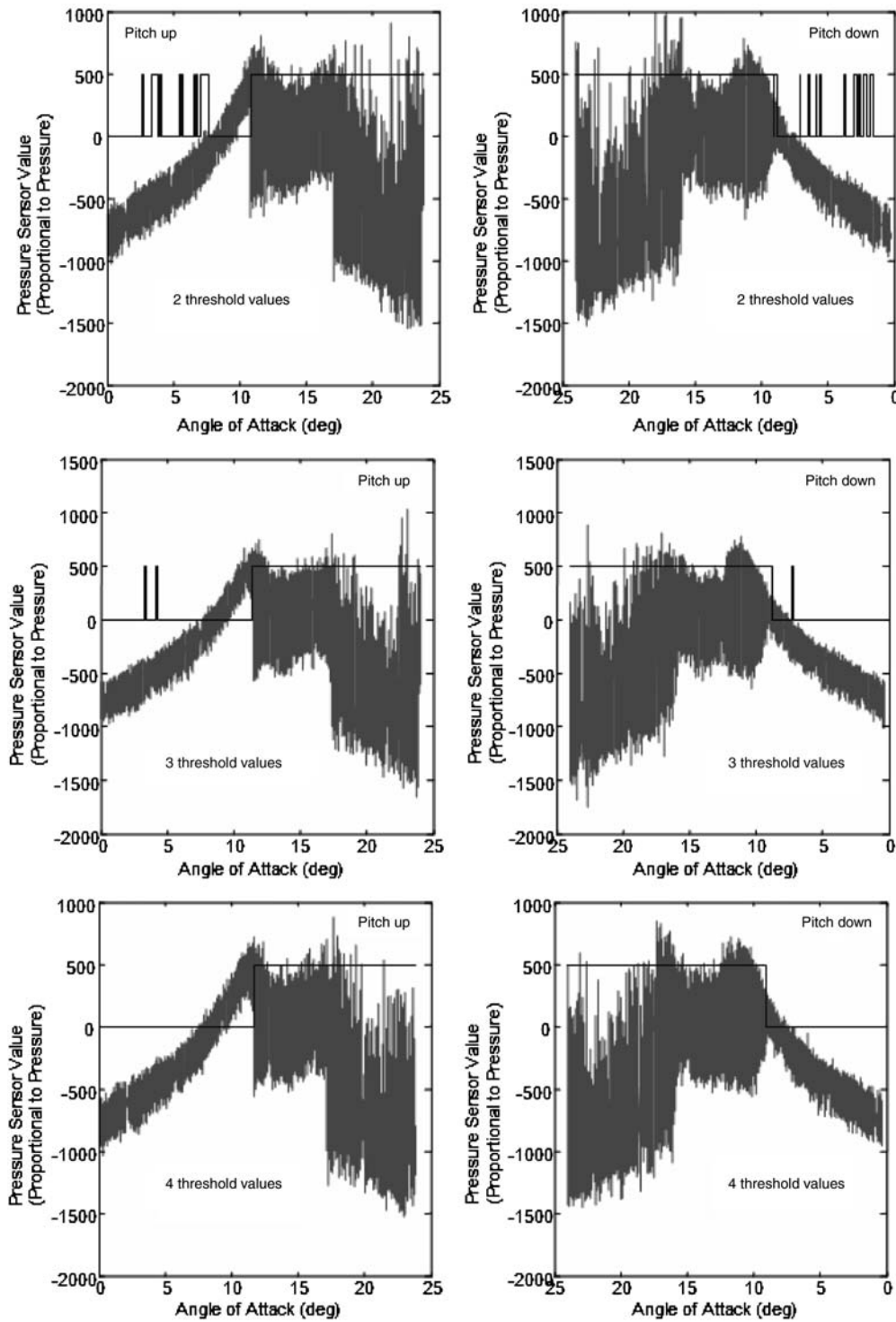


Fig. 16 Comparison of the PASC controller response during the NACA 0015 airfoil pitch-up (left) and pitch-down (right) experiments.

center, and bottom plots, and in Fig. 17, which compares the lift during the 0015 pitch-up experiment using four frequency bins (Fig. 17, left) versus eight 8 bins (Fig. 17, right). Figure 18 compares the effect of 16 bins-8 threshold, 8 bins-4 threshold and 4 bins-4 threshold cases which shows that the controller performance was the same for all except for the 4 bins-4 threshold case.

The results from feedback control experiments of the smart plasma slat are shown in Figs. 19–21. Figure 19 present a comparison of a representative pressure signal as a function of  $\alpha$  during pitch-up (Fig. 19 left) and pitch-down (Fig. 19, right) experiments with plasma off and on. During the pitch up, the PASC controller turns the actuator on at approximately  $\alpha = 12$  deg (2 deg before  $\alpha_{\text{stall}}$ ) and during the pitch down from  $\alpha = 24$  deg; first it turns the actuator on

instantaneously as it detects a stalled condition and then turns the actuator off at approximately  $\alpha = 9$  deg when it senses that the flow is attached and control is not required. Figure 20 shows a spectral power distribution plot of the 0015 pitch-down case with the PASC controller enabled. It shows the difference in amplitude levels over a wide frequency spectrum as the 0015 undergoes a pitch-down motion from  $\alpha = 24$  to 0 deg with the actuator commanded off around  $\alpha = 9$  deg. It was noticed that the angles of attack at which the PASC controller turns the actuator on during pitch up and off during pitch down are different. This was due to the hysteresis in the actuator-induced flow. As some hysteresis in the pressure data was observed during pitching experiments, additional experiments were conducted to investigate the effects of the smart plasma slat on the

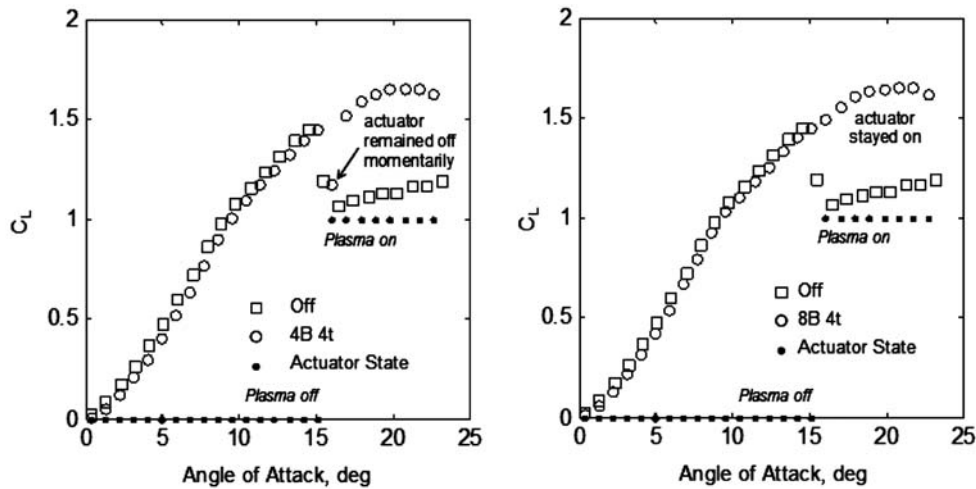


Fig. 17 Comparison of PASC controller response during the NACA 0015 pitch-up experiment using 4-bin 4-threshold (left) and 8-bin 4-threshold (right) settings.

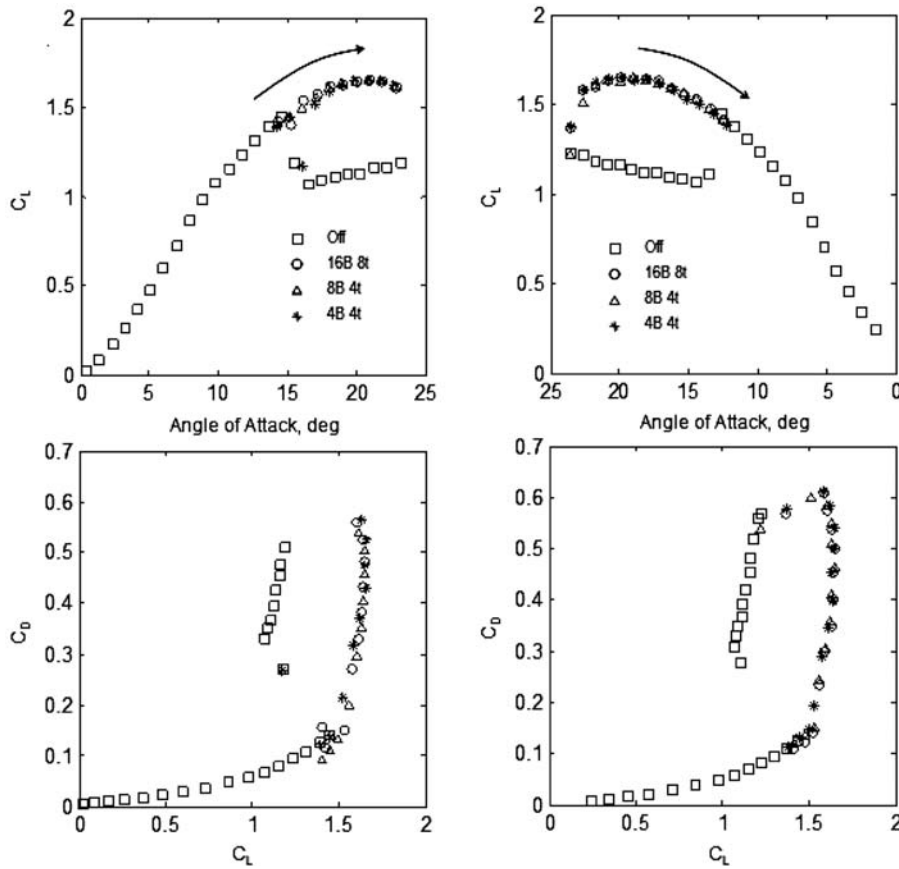


Fig. 18 Comparison of PASC controller response during the NACA 0015 pitch-up (left) and pitch-down (right) experiments using different bin and threshold settings.

stall hysteresis and on lift and drag. The results from these experiments are highlighted in Fig. 21, which shows that stall hysteresis was practically eliminated using the PASC-controlled smart plasma slat.

### Concluding Remarks

Two methods of feedback control for the smart plasma slat application were presented. Both use information from pressure fluctuations measured using a single pressure sensor near the leading edge ( $x/c = 0.05$ ) of an airfoil. Both methods were demonstrated on a NACA 0015 airfoil that used a leading-edge plasma actuator for separation control. The first method (amplitude peak sense and

control) used the detection of a spectral peak in the pressure fluctuations at the unsteady plasma actuator frequency as an indicator of incipient separation. The second method (pressure amplitude sense and control) relied on a smart system that looked at the frequency distribution of energy in the pressure fluctuations to sense incipient separation. In a scenario of decreasing angles of attack from post-stall conditions, where the actuator maintained an attached flow, both feedback control approaches were capable of determining when the flow would naturally reattach, and turned the actuator off. The capabilities of either of the feedback control approaches provide an improvement over simple open-loop control that can conserve flow actuator power in situations where it is limited, or in maximizing the system impact that active flow control can provide.

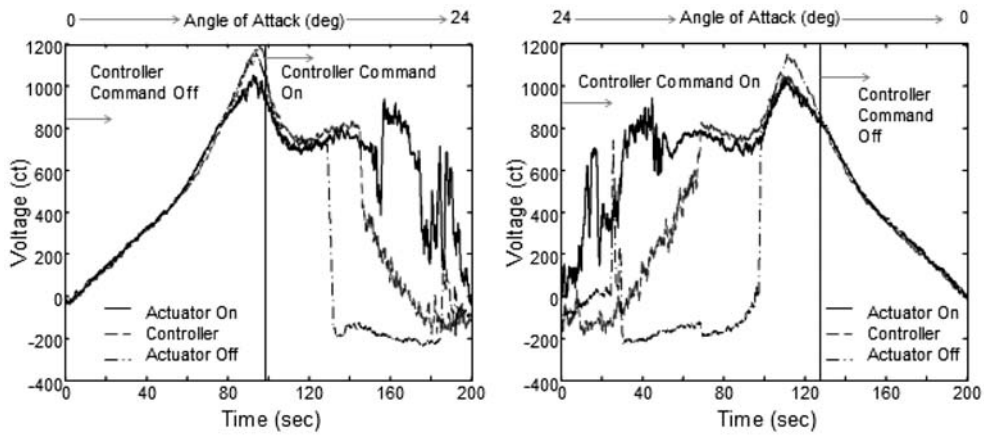


Fig. 19 An overlay plot showing comparisons of a representative pressure signal from 0015 pitch-up (left) and pitch-down (right) experiments with plasma off, plasma on, and using a PASC-enabled feedback controller to drive the plasma actuator.

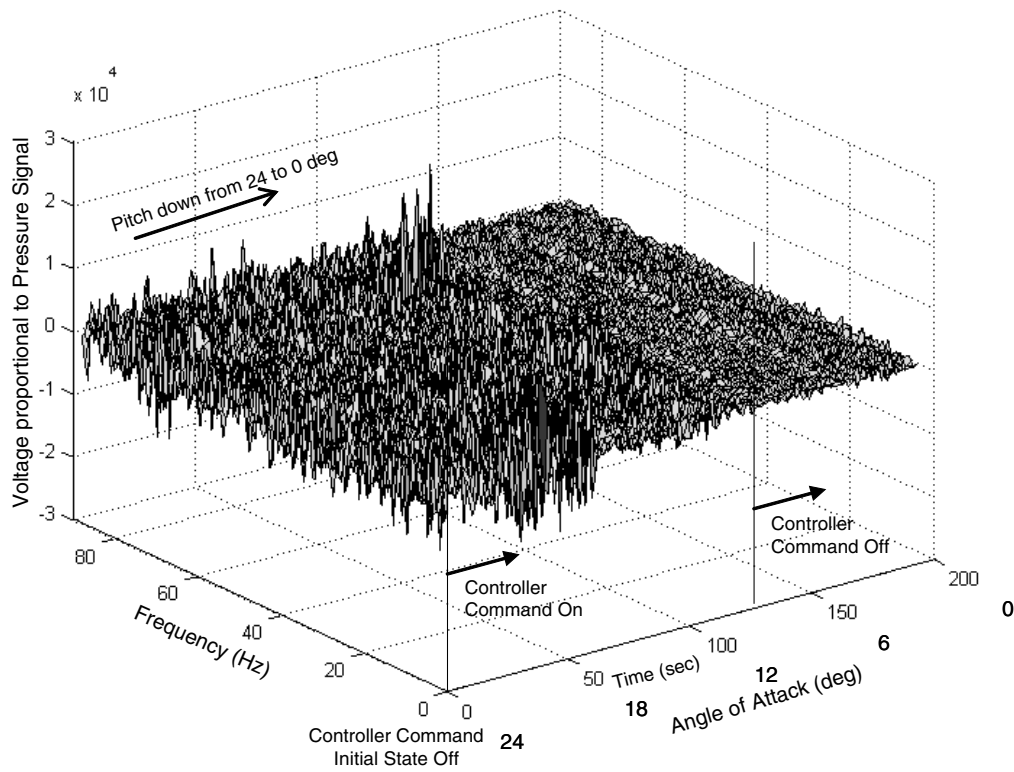


Fig. 20 Spectral power distribution plot from the 0015 pitch-down experiment using the PASC-enabled controller.

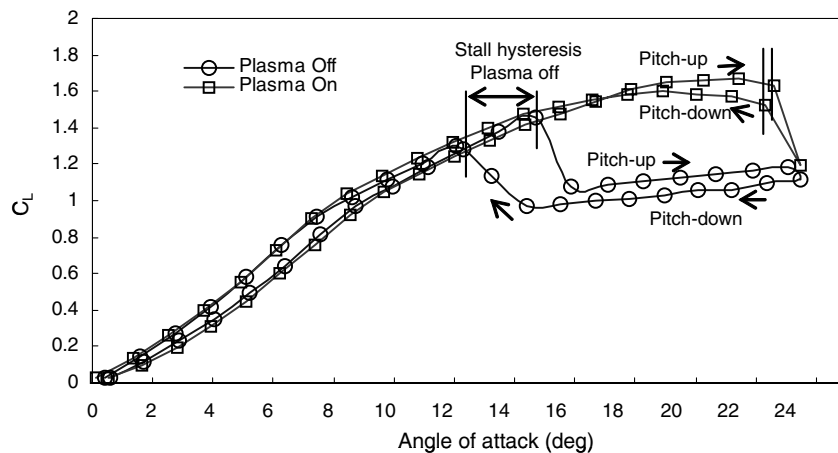


Fig. 21 Overlay of results from feedback control experiments showing near elimination of stall hysteresis on the 0015 using the PASC smart plasma slat.

### Acknowledgment

This work was conducted under a SBIR Phase II Program from the USAF/AFRL, VA, under Contract No. FA8650-04-C-3405 monitored by the USAF Program Manager Charles F. Suchomel.

### References

- [1] Corke, T. C., *Design of Aircraft*, Prentice-Hall, New York, 2002.
- [2] Corke, T. C., He, C., and Patel, M. P., "Plasma Flaps and Slats: An Application of Weakly-Ionized Plasma Actuators," *AIAA Paper 2004-2127*, July 2004.
- [3] Chang, P. K., *Control of Separation*, McGraw-Hill, New York, 1976.
- [4] Gad-el-Hak, M., and Bushnell, D. M., "Separation Control: Review," *Journal of Fluid Engineering*, Vol. 113, March 1991, pp. 5-30.
- [5] Greenblatt, D., and Wygnanski, I., "Control of Separation by Periodic Excitation," *Progress in Aerospace Sciences*, Vol. 37, No. 7, 2000, pp. 487-545.
- [6] Seifert, A., Darabi, A., and Wygnanski, I., "Delay of Airfoil Stall by Periodic Excitation," *Journal of Aircraft*, Vol. 33, No. 4, 1996, pp. 691-698.
- [7] Lin, J. C., Robinson, S. K., McGhee, R. J., and Valarezo, W. O., "Separation Control on High-Lift Airfoils Via Micro-Vortex Generators," *Journal of Aircraft*, Vol. 31, No. 6, 1994, pp. 1317-1323.
- [8] Patel, M. P., Tilmann, C. P., and Ng, T. T., "Active Transparent Stall Control System for Air Vehicles," *Journal of Aircraft*, Vol. 40, No. 5, 2003, pp. 993-997.
- [9] McManus, K. R., Joshi, P. B., Legner, H. H., and Davis, S. J., "Active Control of Aerodynamic Stall Using Pulsed Jet Actuators," *AIAA Paper 1995-2187*, June 1995.
- [10] Corke, T. C., and Post, M., "Overview of Plasma Flow Control: Concepts, Optimization, and Applications," *AIAA Paper 2005-0563*, Jan. 2005.
- [11] Goradia, Suresh H., and Lyman, Victor, "Laminar Stall Prediction and Estimation of  $C_{L(max)}$ ," *Journal of Aircraft*, Vol. 11, No. 9, 1974, pp. 528-536.
- [12] Enloe, L., McLaughlin, T., VanDyken, R., Kachner, Jumper, E., and Corke, T. C., "Mechanisms and Response of a Single Dielectric Barrier Plasma Actuator: Plasma Morphology," *AIAA Journal*, Vol. 42, No. 3, March 2004, pp. 589-594.
- [13] Enloe, L., McLaughlin, T., VanDyken, R., Kachner, Jumper, E., Corke, T. C., Post, M., and Haddad, O., "Mechanisms and Response of a Single Dielectric Barrier Plasma Actuator: Geometric Effects," *AIAA Journal*, Vol. 42, No. 3, March 2004, pp. 595-604.
- [14] Orlov, D. M., and Corke, T. C., "Numerical Simulation of Aerodynamic Plasma Actuator Effects," *AIAA Paper 2005-1083*, Jan. 2005.
- [15] Nelson, C. C., Cain, A. B., Patel, M. P., and Corke, T. C., "Simulation of Plasma Actuators Using the Wind-US Code," *AIAA Paper 2006-0634*, Jan. 2006.
- [16] Orlov, D. M., Corke, T. C., and Patel, M. P., "Electric Circuit Model for the Aerodynamic Plasma Actuator," *AIAA Paper 2006-1206*, Jan. 2006.
- [17] Corke, T. C., Cavalieri, D., and Matlis, E., "Boundary Layer Instability on a Sharp Cone at Mach 3.5 with Controlled Input," *AIAA Journal*, Vol. 40, No. 5, 2001, pp. 1015-1018.
- [18] Corke, T. C., Jumper, E., Post, M., Orlov, D. and McLaughlin, T., "Application of Weakly-Ionized Plasmas as Wing Flow-Control Devices," *AIAA Paper 2002-0350*, Jan. 2002.
- [19] Huang, J., Corke, T. C., and Thomas, F., "Plasma Actuators for Separation Control of Low-Pressure Turbine Blades," *AIAA Paper 2003-1027*, *AIAA Journal* (to be published).
- [20] Post, M., and Corke, T. C., "Separation Control on High Angle of Attack Airfoil Using Plasma Actuators," *AIAA Journal*, Vol. 42, No. 11, 2004, pp. 2177-2184; also *AIAA Paper 2003-1024*.
- [21] Corke, T. C., and Matlis, E., "Phased Plasma Arrays for Unsteady Flow Control," *AIAA Paper 2000-2323*, Jan. 2000.
- [22] Post, M., and Corke, T. C., "Separation Control Using Plasma Actuators—Stationary and Oscillating Airfoils," *AIAA Paper 2004-0841*, 2004.
- [23] Corke, T. C., Mertz, B., and Patel, M. P., "Plasma Flow Control Optimized Airfoil," *AIAA Paper 2006-1208*, Jan. 2006.
- [24] Patel, M. P., Ng, T. T., Vasudevan, S., Corke, T. C., and He, C., "Plasma Actuators for Hingeless Aerodynamic Control of an Unmanned Air Vehicle," *AIAA Paper 2006-3495*, June 2006.
- [25] Broeren, A. P., and Bragg, M. B., "Flowfield Measurements over an Airfoil During Natural Low-Frequency Oscillation near Stall," *AIAA Journal*, Vol. 37, No. 1, 1999, pp. 130-132.